**Electronic supplementary information**

# Metal shields with crystallographic discrepancies incorporated into integrated architectures for stable lithium metal batteries

Ki-Yeop Cho, Sungjun Cho, Gun Young Jung*, and KwangSup Eom*

*School of Materials Science and Engineering, Gwangju Institute of Science and Technology (GIST), 123 Cheomdangwagi-ro, Buk-gu, Gwangju 61005, Republic of Korea*

*Corresponding authors, E-mails: Gun Young Jung (gyjung@gist.ac.kr) and KwangSup Eom (keom@gist.ac.kr)

**Experimental Section/Methods**

*Sample preparation*: Ti foils with a thickness of 15 μm were employed as substrates for Li electrodeposition to investigate Li electrodeposition behavior on Ti surfaces. Before electrodeposition, the as-received Ti foils were successively degreased by acetone, ethanol and distilled water under sonication. After drying, the degreased Ti foils were pretreated with an acid mixture composed of hydrofluoric acid, nitric acid and distilled water (1:10:89 by volume) for 2 min to remove naturally formed dense surface oxides, and then, the Ti foils directly served as the substrates for subsequent electrodeposition. Eighteen micrometer-thick commercial Cu foils were utilized as substrates for both Li electrodeposition and thin film evaporation. Before the experiments, the Cu foils were treated with 0.5 M $H_2SO_4$ solution for 10 min to remove native Cu oxides, followed by successive washing in distilled water and acetone. Various metal films (M@Cu, M=Ni, Cr, and Ti) were formed on the surface of Cu foils by physical evaporation methods, and the thickness of the films was controlled to 300 nm. Metal-patterned Cu substrates (*p*-M@Cu, M=Ni, Cr, and Ti) were fabricated by means of photolithography, and the fabrication process is depicted in **Figure S36**. First, a photoresist (AZ GXR 601) was spin-coated on the surface of Cu foils to obtain resist patterns. Then, the patterned Cu foils served as substrates for subsequent metal evaporation. Finally, the *p*-M@Cu substrates were obtained with a lift-off process by dipping into a solution (EKC 830) for several minutes. For the wet-chemical etching process, commercially available Cu etchant (CE-100) was used as a chloride bath without any pretreatment. Cu foils patterned with photoresist or Ti based on the abovementioned method directly served as etching objects to fabricate the *p*-CuCl@Cu and *p*-Ti_CuCl@Cu architectures. After the wet-etching process, the etched substrates were cleaned with distilled water and ethanol before the subsequent experiments.

*Materials characterization*: All field-emission scanning electron microscopy (FE-SEM) images were collected by a Verios 5 UC (*Thermo Fisher Scientific*) equipped with an energy dispersive spectrometer (Ultim Max 65, *Oxford*) or JSM-7500F (*Jeol*). X-ray diffraction patterns were obtained at a scanning rate of 5° $min^{-1}$ by using an X-ray diffractometer (Smartlab, *Rigaku*). An X-ray photoelectron spectrometer (NEXSA, *Thermo Fisher Scientific*) was used to investigate the valence states of the metals in the thin films.

*Electrochemical measurements:* CR2032-type coin cells were exploited to investigate the electrodeposition behavior of Li and collect electrochemical measurements. The coin cells

were assembled in a glove box in which the moisture and oxygen contents were below 1 ppm. The half-cell consisted of a prepared substrate as a working electrode, a polypropylene film (Celgard 2400) as a separator and a lithium chip as a reference electrode. To prepare ether-based electrolytes, a solution mixture of 1,3-dioxolane (DOL) and 1,2-dimetoxyethane (DME) was prepared as electrolyte solvents (1:1 by volume). Then, 1 M lithium bis(trifluoromethanesulfonyl)imide (LiTFSI) was dissolved in the solution as Li salts, and 2 wt% lithium nitrates were mixed as electrolyte additives. All electrochemical measurements were conducted by using a battery cycler (WBCS3000, *WonATech*) operating inside a thermohygrostat in which the inside temperature was maintained at 27 ℃. Electrochemical impedance spectroscopy (EIS) of symmetric cells was performed with a voltage amplitude of 10 mV over a frequency range from $10^{-1}$ Hz to $10^{6}$ Hz by a frequency analyzer (Solartron 1470E/1400 Cell test systems, *Solartron Analytical*). The symmetric cells consisted of two lithium metal anodes electrodeposited on each of the substrates at a current density of 1 mA $cm^{-2}$ at 1 mAh $cm^{-2}$. The Z-view program (*Scribner Associates*) was employed to fit the obtained Nyquist plots. In full-cell tests, a $LiFePO_4$-based cathode was used for the fabrication of anode-free lithium metal batteries. The cathode was prepared through a slurry casting process, and the slurry was composed of 80 wt% $LiFePO_4$ powder (*MTI corporation*), 10 wt% conductive carbon (Super C65, *Timcal*) and 10 wt% binder (polyvinylidene fluoride (PVDF), *MTI corporation*). The full cells were cycled in a voltage range from 3.0 V to 4.0 V at a current density of C/3 after 1 cycle of the activation process at a current density of C/20 (1C = 170 mAh $g^{-1}$).

## Supplementary Figures

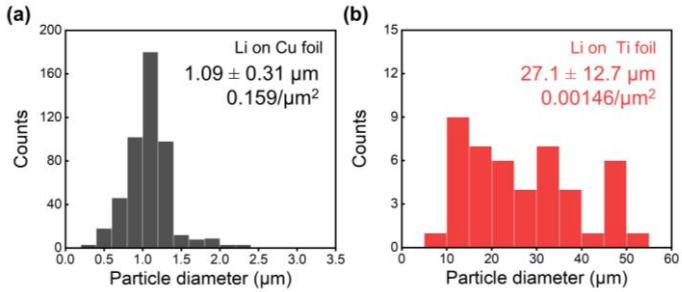


**Fig. S1** Histograms of Li particle sizes formed on (a) Cu foils and (b) Ti foils. Each of histograms is measured based on Fig.1b and c, respectively.

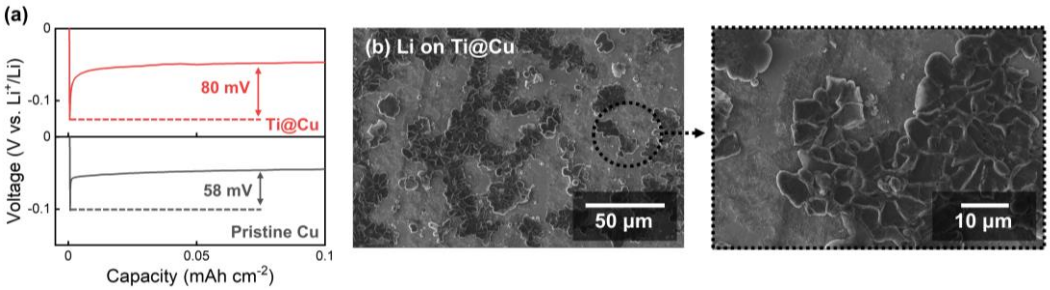


**Fig. S2** (a) Capacity-voltage curves for galvanostatic deposition of Li on Cu foils and Ti-coated Cu foils (Ti@Cu). (b) FE-SEM surface images of electrodeposited Li on Ti-coated Cu foils (Ti@Cu). The electrodeposition was conducted at a current density of 0.2 mA $cm^{-2}$ for a Li capacity of 0.1 mAh $cm^{-2}$.

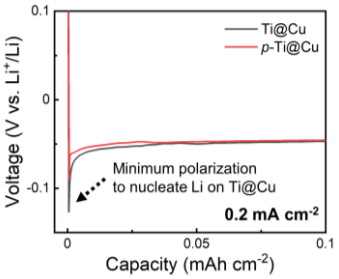


**Fig. S3** Comparison of capacity-voltage curves for the Li electrodeposition reaction on Ti-coated Cu foils (Ti@Cu) and Ti-patterned Cu foils (*p*-Ti@Cu). The electrodeposition was conducted at a current density of 0.2 mA $cm^{-2}$ for a Li capacity of 0.1 mAh $cm^{-2}$.

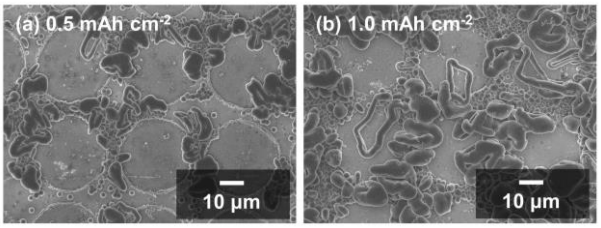


**Fig. S4** FE-SEM surface images of Ti-patterned Cu foils (*p*-Ti@Cu) after electrodeposition of Li at a current density of 0.2 mA $cm^{-2}$ for different Li capacities of (a) 0.5 mAh $cm^{-2}$ and (b) 1.0 mAh $cm^{-2}$.

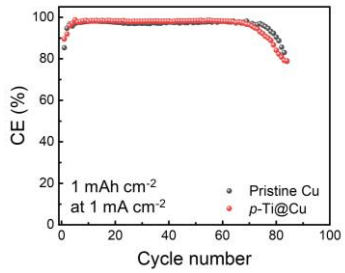


**Fig. S5** Coulombic efficiency variations during the repeated electrodeposition/dissolution reaction of Li on Ti-patterned Cu foils (*p*-Ti@Cu). The measurement was conducted at a current density of 1 mA $cm^{-2}$ for a Li capacity of 1 mAh $cm^{-2}$.

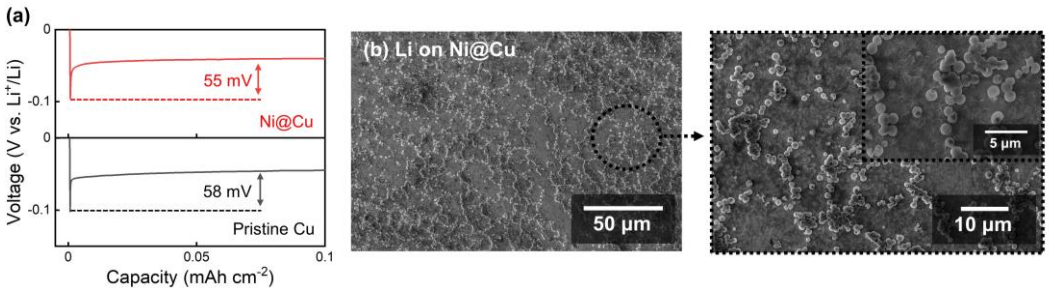


**Fig. S6** (a) Capacity-voltage curves for galvanostatic deposition of Li on Cu foils and Ni-coated Cu foils (Ni@Cu). (b) FE-SEM surface images of electrodeposited Li on Ni-coated Cu foils (Ni@Cu). The electrodeposition was conducted at a current density of 0.2 mA $cm^{-2}$ for a Li capacity of 0.1 mAh $cm^{-2}$.

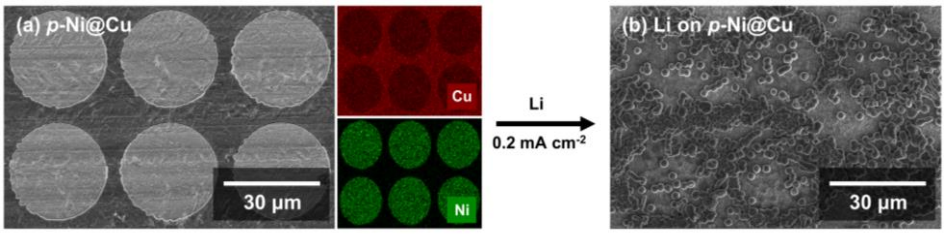


**Fig. S7** (a) FE-SEM surface image and EDS mapping results of Ni-patterned Cu foils (*p*-Ni@Cu) and (b) a corresponding FE-SEM image of Li electrodeposited at a current density of 0.2 mA $cm^{-2}$ for a Li capacity of 0.1 mAh $cm^{-2}$.

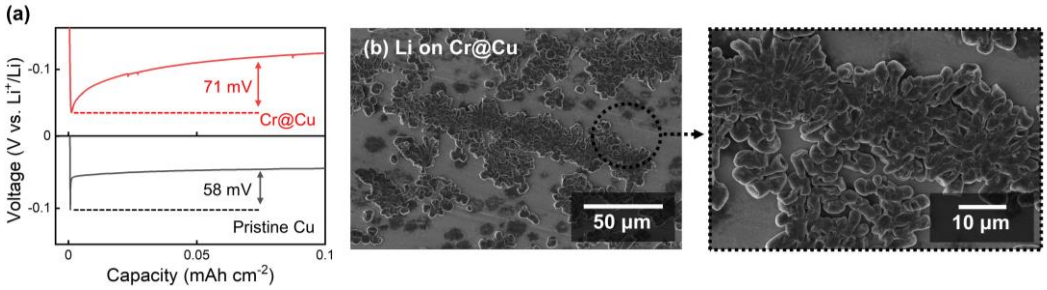


**Fig. S8** (a) Capacity-voltage curves for galvanostatic deposition of Li on Cu foils and Cr-coated Cu foils (Cr@Cu). (b) FE-SEM surface images of electrodeposited Li on Cr-coated Cu foils (Cr@Cu). The electrodeposition was conducted at a current density of 0.2 mA $cm^{-2}$ for a Li capacity of 0.1 mAh $cm^{-2}$.

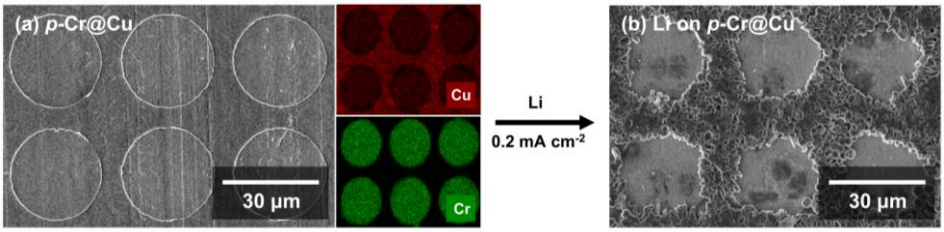


**Fig. S9** (a) FE-SEM surface image and EDS mapping results of Cr-patterned Cu foils (*p*-Cr@Cu) and (b) a corresponding FE-SEM image of Li electrodeposited at a current density of 0.2 mA $cm^{-2}$ for a Li capacity of 0.1 mAh $cm^{-2}$.

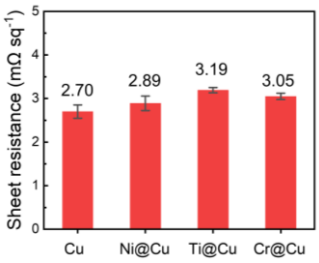


**Fig. S10** Sheet resistance values of various substrate. The error bars are based on the measurement results of 5 samples.

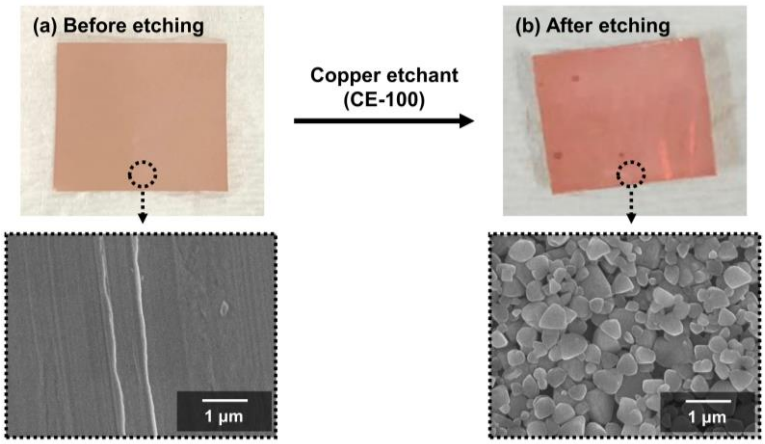


**Fig. S11** Optical and FE-SEM surface images of Cu foils (a) before and (b) after wet-chemical etching.

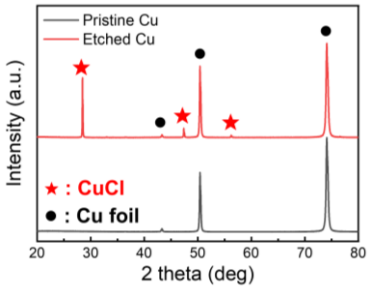


**Fig. S12** X-ray diffraction patterns of Cu foils before and after wet-chemical etching.

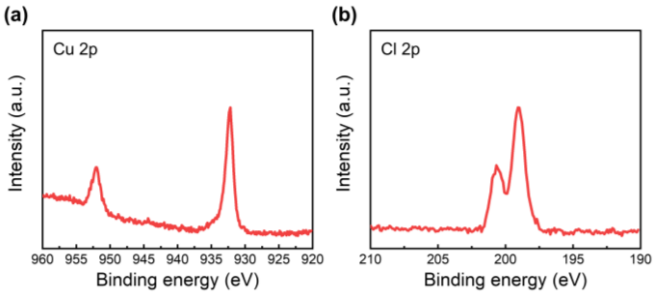


**Fig. S13** X-ray photoelectron spectra of (a) Cu 2p and (b) Cl 2p for etched Cu foils.

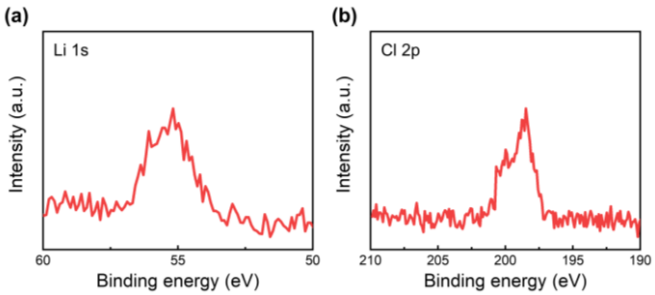


**Fig. S14** X-ray photoelectron spectra of (a) Li 1s and (b) Cl 2p for etched Cu foils after electrodeposition of Li at a current density of 1 mA $cm^{-2}$ for 1 mAh $cm^{-2}$.

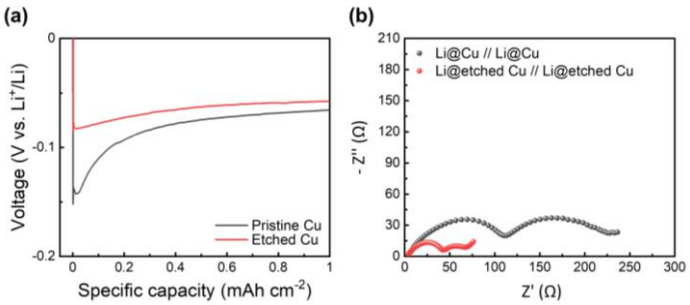


**Fig. S15** (a) Comparison of capacity-voltage curves for the electrodeposition reaction of Li on pristine Cu and etched Cu. (b) Nyquist plots for electrochemical impedance measurements on symmetric cells. All electrodeposition of Li was conducted at a current density of 1 mA $cm^{-2}$ for a Li capacity of 1 mAh $cm^{-2}$.

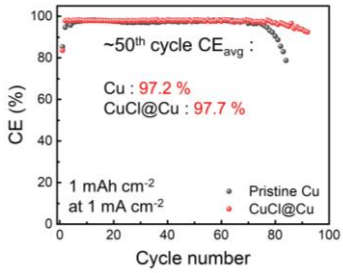


**Fig. S16** Coulombic efficiency variations during the repeated electrodeposition/dissolution reaction of Li on etched Cu foils (CuCl@Cu). The measurement was conducted at a current density of 1 mA $cm^{-2}$ for a Li capacity of 1 mAh $cm^{-2}$.

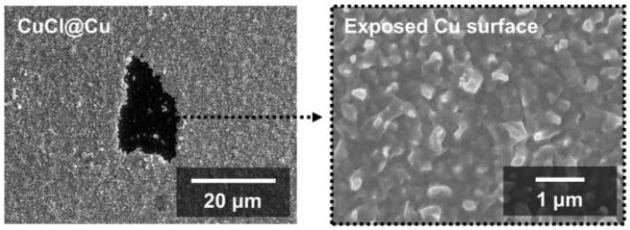


**Fig. S17** FE-SEM surface images of etched Cu foils and exposed Cu surface underneath CuCl coating layers.

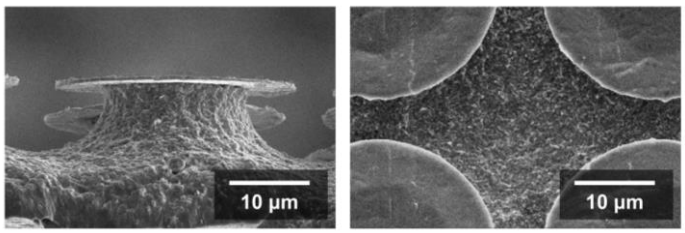


**Fig. S18** FE-SEM cross-sectional and surface images of the *p*-Ti_CuCl@Cu after lithiation reaction of CuCl to 0 V vs. $Li^+$/Li.

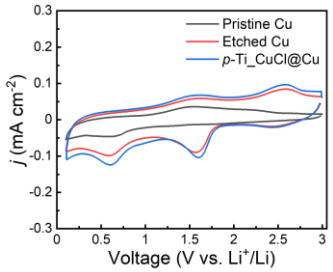


**Fig. S19** Cyclic voltammetry (CV) results of pristine Cu, etched Cu and *p*-Ti_CuCl@Cu.

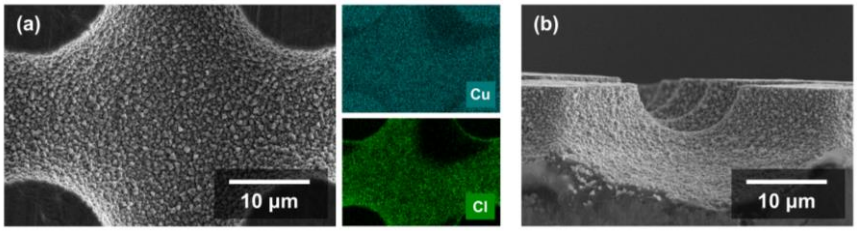


**Fig. S20** (a) FE-SEM surface images and elemental mapping images of the *p*-CuCl@Cu substrates, and (b) a corresponding cross-sectional image.

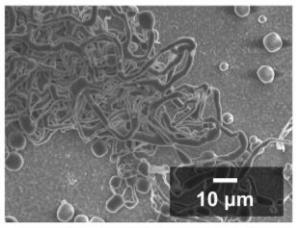


**Fig. S21** FE-SEM surface image of pristine Cu after electrodeposition of Li at a current density of 1.0 mA $cm^{-2}$ for a Li capacity of 1.0 mAh $cm^{-2}$.

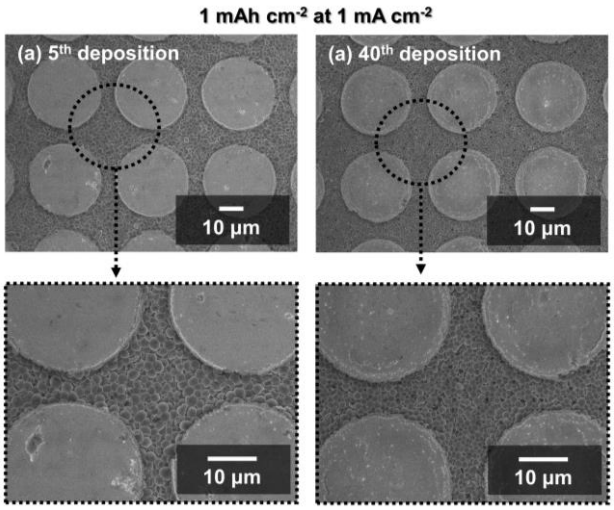


**Fig. S22** FE-SEM surface images of *p*-Ti_CuCl@Cu after the (a) 5$^{th}$ and (b) 40$^{th}$ deposition cycles of Li during repeated electrodeposition/dissolution cycles.

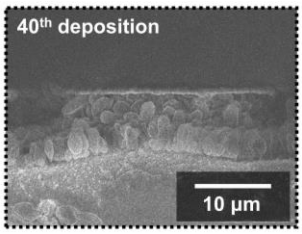


**Fig. S23** FE-SEM cross-sectional image of *p*-Ti_CuCl@Cu after 40$^{th}$ deposition cycles of Li during repeated electrodeposition/dissolution cycles.

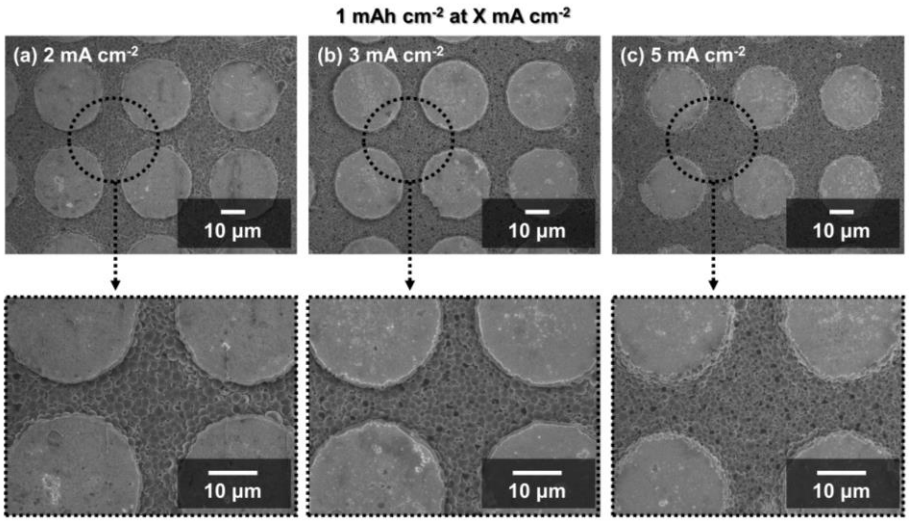


**Fig. S24** FE-SEM surface images of *p*-Ti_CuCl@Cu after 1 mAh $cm^{-2}$ Li electrodeposition at various current densities of (a) 2 mA $cm^{-2}$, (b) 3 mA $cm^{-2}$, and (c) 5 mA $cm^{-2}$.

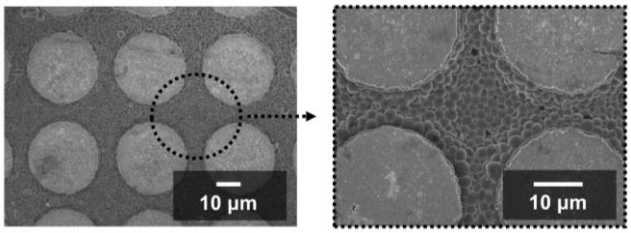


**Fig. S25** FE-SEM surface images of the *p*-Ti_CuCl@Cu after 2 mAh $cm^{-2}$ of Li electrodeposition at a current density of 1 mA $cm^{-2}$.

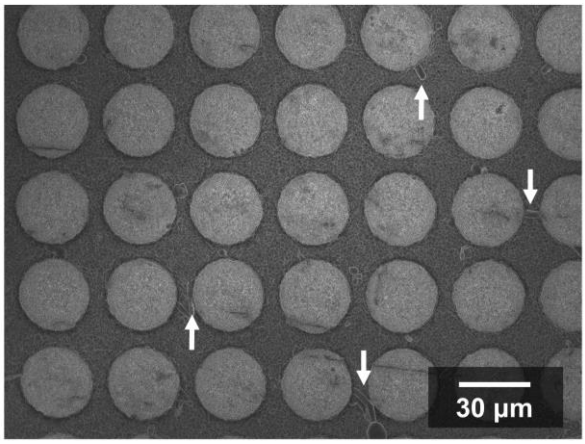


**Fig. S26** low magnification FE-SEM surface image of the *p*-Ti_CuCl@Cu after 2 mAh $cm^{-2}$ of Li electrodeposition at a current density of 1 mA $cm^{-2}$ (The white arrows are indicative of Li dendrites).

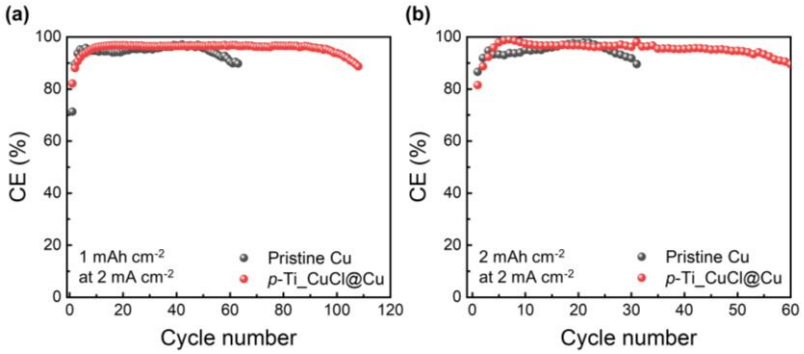


**Fig. S27** Comparison in Coulombic efficiency variations during the repeated electrodeposition/dissolution reaction of Li on pristine Cu and *p*-Ti_CuCl@Cu with different electrochemical loads. The measurements were conducted (a) at a current density of 2 mA $cm^{-2}$ for a Li capacity of 1 mAh $cm^{-2}$, and (b) at a current density of 2 mA $cm^{-2}$ for a Li capacity of 2 mAh $cm^{-2}$.

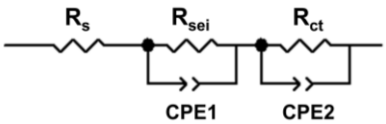


**Fig. S28** A equivalent circuit for analysis of the Nyquist plots obtained through electrochemical impedance spectroscopy ($R_s$: solution resistances, $R_{sei}$: resistances for solid-electrolyte interphases (SEIs), $R_{ct}$: charge transfer resistances, CPE: constant phase elements for corresponding resistive processes).

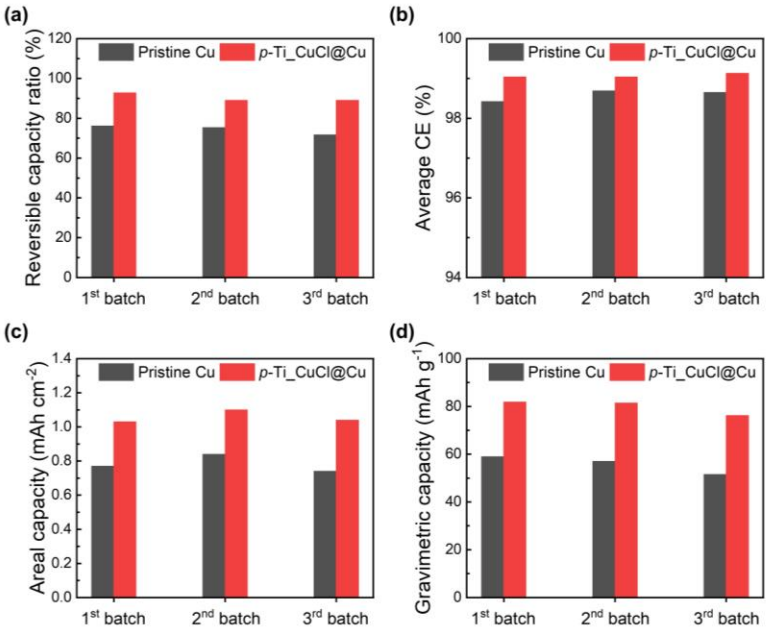


**Fig. S29** Comparison of cyclic stability testing on 3 pairs of AFLMBs employing pristine Cu and *p*-Ti_CuCl@Cu substrates. (a) Reversible capacity ratio (discharge capacity to corresponding charge capacity at activation cycle with a current density of C/20), (b) average CE values during 100 cycles, residual capacity values at 50$^{th}$ cycle in form of (c) areal capacities and (d) gravimetric capacities.

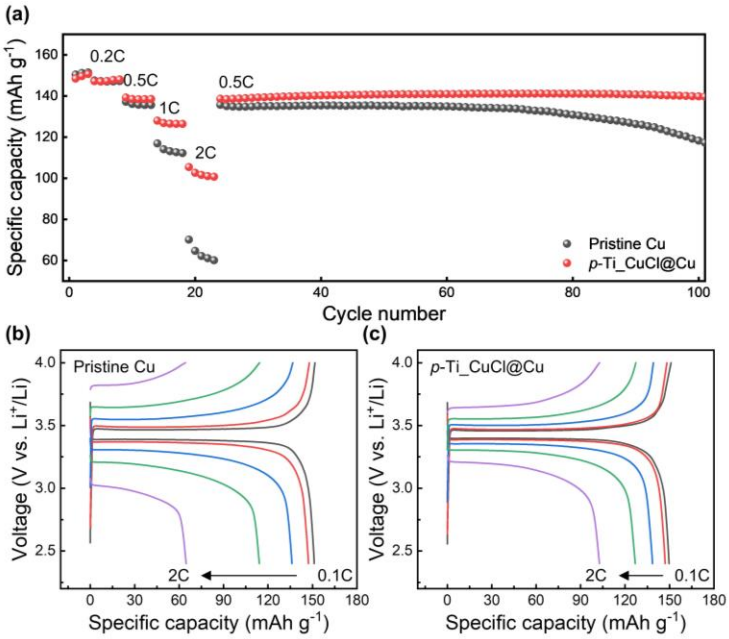


**Fig. S30** Performance comparison of LMBs with a low N/P ratio of 1. Each of cells are composed of electrodeposited LMA on pristine Cu or *p*-Ti_CuCl@Cu as an anode and $LiFePO_4$ as a cathode. (a) Cyclic stability, and (b), (c) polarization curves of the cell employing (b) Li on pristine Cu and (c) Li on *p*-Ti_CuCl@Cu.

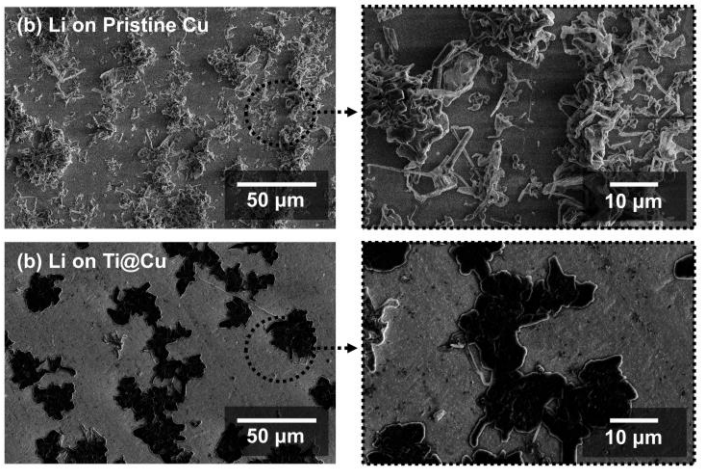


**Fig. S31** FE-SEM images of electrodeposited Li on (a) pristine Cu and (b) Ti-coated Cu foil (Ti@Cu) in a carbonate electrolyte with a composition of 1 M $LiPF_6$ in EC/DEC (1:1 by volume) with 10 wt% FEC. The electrodeposition was conducted at a current density of 0.2 mA $cm^{-2}$ for a Li capacity of 0.1 mAh $cm^{-2}$.

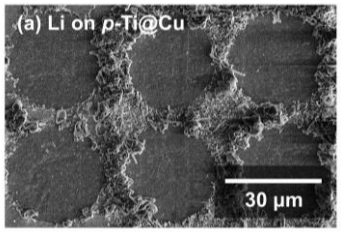


**Fig. S32** FE-SEM image of the Ti-patterned Cu foils (*p*-Ti@Cu) after electrodeposition of Li in a carbonate electrolyte with a composition of 1 M $LiPF_6$ in EC/DEC (1:1 by volume) with 10 wt% FEC. The electrodeposition was conducted at a current density of 0.2 mA $cm^{-2}$ for a Li capacity of 0.1 mAh $cm^{-2}$.

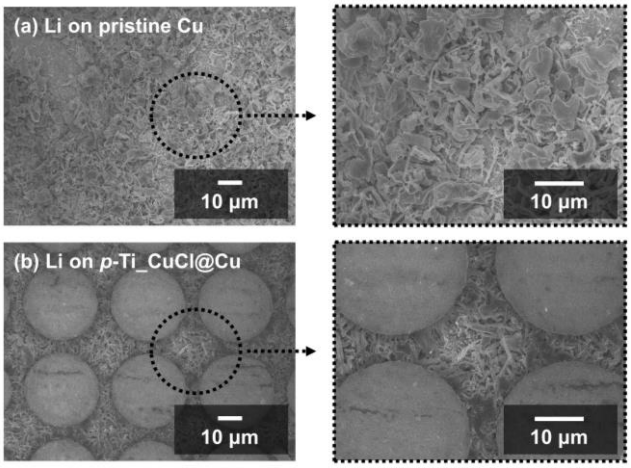


**Fig. S33** FE-SEM surface images of electrodeposited Li on (a) pristine Cu and (b) *p*-Ti_CuCl@Cu in a carbonate electrolyte with a composition of 1 M $LiPF_6$ in EC/DEC (1:1 by volume) with 10 wt% FEC. The electrodeposition of Li was conducted for a Li capacity of 1 mAh $cm^{-2}$ at a current density of 1 mA $cm^{-2}$).

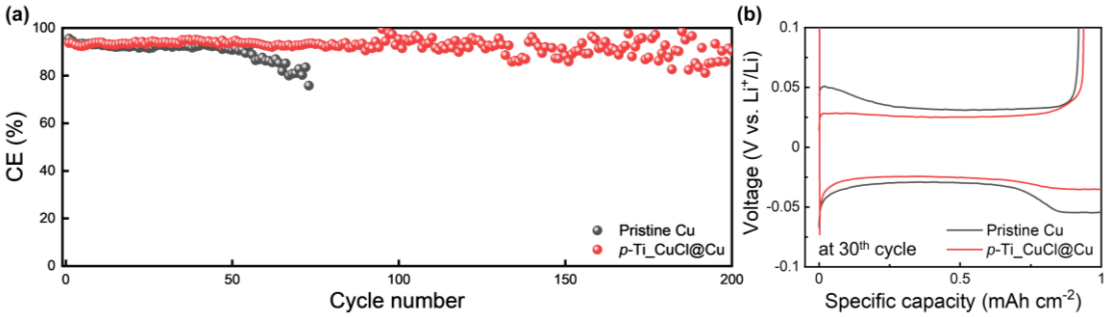


**Fig. S34** (a) Coulombic efficiency variations during the repeated electrodeposition/dissolution reaction of Li on pristine Cu and *p*-Ti_CuCl@Cu substrates in carbonate electrolytes with a composition of 1 M $LiPF_6$ in EC/DEC (1:1 by volume) with 10 wt% FEC. (b) Polarization curves of the substrates at the 30$^{th}$ cycle in (a). The measurement was conducted at a current density of 1 mA cm$^{-2}$ for a Li capacity of 1 mAh cm$^{-2}$.

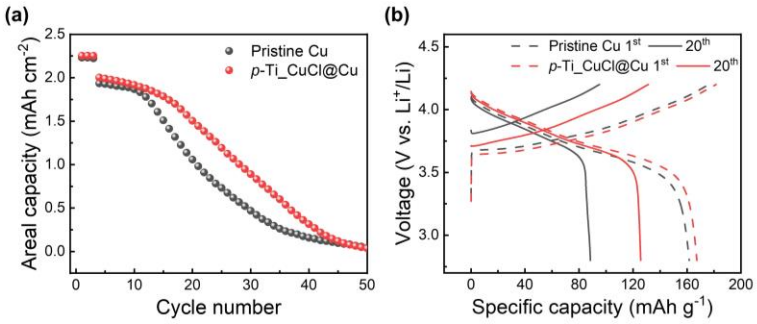


**Fig. S35** Comparison of AFLMB full-cell performances employing pristine Cu and *p*-Ti_CuCl@Cu as hosts for Li deposition and $LiNi_{8.5}Co_{1.5}Al_{0.35}O_2$ as cathodes. (a) Cycling performances at a current density of 0.5C after 3 cycles of activation process at a current density of C/10, and (b) corresponding polarization curves of each cell.

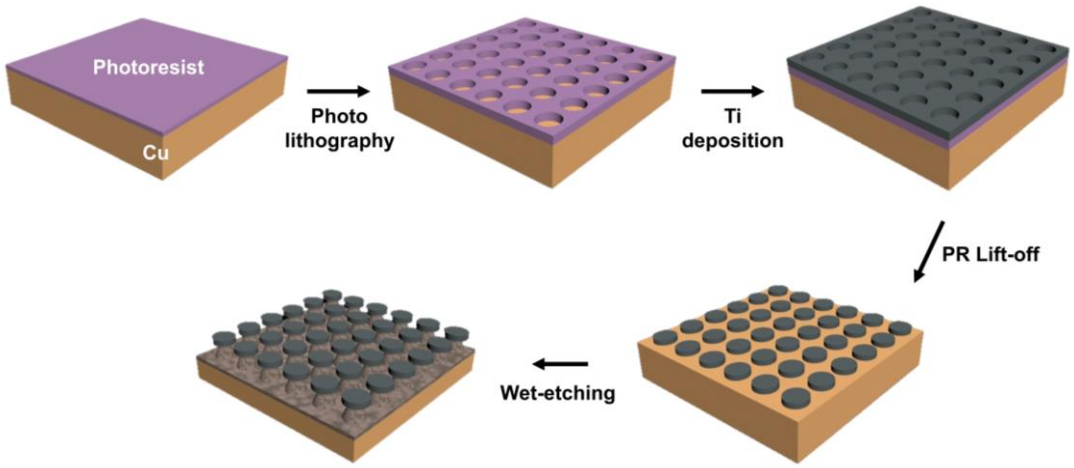


**Fig. S36** Experimental process for fabrication of metal-patterned Cu and *p*-Ti_CuCl@Cu.

## Supplementary tables

| Element | Crystal structure | Lattice parameter (pm) | Misfit (%) |
|---|---|---|---|
| Cu | *Faced-Centered Cubic (FCC)* | 361 | 2.8 |
| Ni | | 354 | 0.8 |
| Li | *Body-Centered Cubic (BCC)* | 351 | 0 |
| V | | 304 | 15.5 |
| Mo | | 314 | 11.8 |
| W | | 316 | 11.1 |
| Cr | | 290 | 21.0 |
| Ti | *Hexagonal Closed Packed (HCP)* | 295 | 19 |
| Zr | | 323 | 8.7 |
| Sc | | 330 | 6.4 |
| Y | | 367 | 4.4 |

**Table S1** Crystallographic characteristics of metallic elements unable to form solid solutions or alloy with Li, and their lattice misfit values with BCC lithium.

## Supplementary notes

*Gibbs free energy changes for heterogeneous nucleation of Li*

The Gibbs free energy ($\Delta G_{nuc.}$) required to form spherical Li nuclei with a radius ($r$) on a heterogeneous surface can be expressed as follows[1,2]:

$$\Delta G_{nuc.} = \Delta G_{bulk} + \Delta G_{surf.} \quad (1)$$

$$\Delta G_{nuc.} = \left(\frac{4}{3}\pi r^3 \Delta G_v + 4\pi r^2 \gamma\right) \cdot \left(\frac{2-3\cos\theta+\cos^3\theta}{4}\right) \quad (2)$$

, where $\Delta G_v$, $\gamma$ and $\Theta$ represent the free energy change per volume, the surface energy of the Li/electrolyte interface and the wetting angle, respectively. The critical radius of nuclei ($r^*$) and Gibbs free energy ($\Delta G_{nuc}^*$) are as follows:

$$r^* = \frac{2\gamma}{\Delta G_v} \quad (3)$$

$$\Delta G_{nuc.}^* = \frac{16\pi\gamma^3}{3\Delta G_v^2} \cdot \left(\frac{2-3\cos\theta+\cos^3\theta}{4}\right) \quad (4)$$

Based on the above relationships, it can be seen that the critical radius of Li nuclei is independent of the substrate. However, the $\Delta G_{nuc}^*$ necessary to form Li nuclei with a radius $r^*$ is a function of the surface energy of Li ($\gamma$) and the wetting angles ($\Theta$, where $0° \leq \Theta \leq 180°$). In our case, the free energy changes would not vary much due to the surface energy of Li, given the identical interfacial environment arising from the same electrolyte[3]. Hence, the Gibbs free energy changes could be dictated by the wetting properties that can vary with the interfacial energy between substrate and Li. In other words, the Gibbs free energy changes required for Li nucleation can be affected by the interfacial energy. Lower interfacial energy (perfect wetting, $\Theta = 0°$) leads to heterogeneous nucleation, while higher interfacial energy (poor wetting, $\Theta = 180°$) requires larger free energy changes comparable to the energy for homogeneous nucleation.

## References


1 W. Plieth, *Electrochemistry for materials science*, Elsevier, Amsterdam ; Boston, 1st ed., 2008.

2 A. Pei, G. Zheng, F. Shi, Y. Li and Y. Cui, *Nano Lett.*, 2017, **17**, 1132–1139.

3 D. T. Boyle, S. C. Kim, S. T. Oyakhire, R. A. Vilá, Z. Huang, P. Sayavong, J. Qin, Z. Bao and Y. Cui, *J. Am. Chem. Soc.*, 2022, **144**, 20717–20725.